Rigorous Solutions of Scattering Problems Involving Red Blood Cells

Özgür Ergül*, Ayça Arslan-Ergül†, Levent Gürel‡§

*Department of Mathematics and Statistics
†Strathclyde Institute of Pharmacy and Biomedical Sciences
University of Strathclyde, Glasgow, UK

‡Department of Electrical and Electronics Engineering
§Computational Electromagnetics Research Center (BiLCEM)
Bilkent University, TR-06800, Bilkent, Ankara, Turkey

Abstract—We present rigorous solutions of scattering problems involving healthy red blood cells (RBCs) and diseased RBCs with deformed shapes. Scattering cross-section (SCS) values for different RBC shapes and different orientations are obtained accurately and efficiently using a sophisticated simulation environment based on the electric and magnetic current combined-field integral equation and the multilevel fast multipole algorithm. Using SCS values, we determine strict guidelines to distinguish deformed RBCs from healthy RBCs and to diagnose related diseases.

I. INTRODUCTION

Scattering from red blood cells (RBCs) has attracted the interest of many researchers since scattering properties of RBCs can provide essential information for the diagnosis of various diseases. Electromagnetic scattering or transmission characteristics of RBCs for different material properties, illumination angles, and frequencies can be found in the literature [1]–[9]. On the other hand, previous studies mostly focused on the simulation of healthy RBCs, and less attention has been paid to diseased RBCs with deformed shapes. In this paper, we present a comparative study of scattering from healthy RBCs and deformed RBCs, particularly spherocytes, microcytes, macrocytes, and sickle cells. Using a robust simulation environment based on the electric and magnetic current combined-field integral equation (JMCFIE) [10] and the multilevel fast multipole algorithm (MLFMA) [11], scattering problems involving different RBC shapes and different orientations are solved accurately and efficiently. By comparing computational scattering cross-section (SCS) values obtained for different RBC shapes, we determine well-defined guidelines to diagnose various diseases.

II. SIMULATION ENVIRONMENT

Scattering problems involving RBCs can be formulated accurately with JMCFIE [10]. Discretization of JMCFIE with the Rao-Wilton-Glisson (RWG) functions [12] on planar triangles leads to $2N \times 2N$ well-conditioned matrix equations in the form of

$$\begin{bmatrix} \bar{\bar{Z}}_{11} & \bar{\bar{Z}}_{12} \\ \bar{\bar{Z}}_{21} & \bar{\bar{Z}}_{22} \end{bmatrix} \cdot \begin{bmatrix} a_J \\ a_M \end{bmatrix} = \begin{bmatrix} v_1 \\ v_2 \end{bmatrix}, \qquad (1)$$

where $\bar{\bar{Z}}_{11} = \bar{\bar{Z}}_{22} = \bar{\bar{I}} + \bar{\bar{Z}}_D$ and $\bar{\bar{I}}$ is a sparse Gram matrix involving well-tested identity operators. As detailed in [10], $\bar{\bar{Z}}_{12}$, $\bar{\bar{Z}}_{21}$, and $\bar{\bar{Z}}_D$ involve discretized integro-differential operators derived for inner and outer media, as well as weakly-tested identity operators. The matrix equation in (1) can be solved efficiently by using iterative algorithms [13]. Nevertheless, accurate discretizations of RBCs at realistic frequencies lead to large matrix equations and we need to employ MLFMA to accelerate the matrix-vector multiplications required by iterative solvers without deteriorating the accuracy of results.

Using MLFMA, matrix-vector multiplications involving the $2N \times 2N$ matrix in (1), i.e.,

$$\begin{bmatrix} y_1 \\ y_2 \end{bmatrix} = \begin{bmatrix} \bar{\bar{Z}}_{11} & \bar{\bar{Z}}_{12} \\ \bar{\bar{Z}}_{21} & \bar{\bar{Z}}_{22} \end{bmatrix} \cdot \begin{bmatrix} x_1 \\ x_2 \end{bmatrix}, \qquad (2)$$

can be performed efficiently in $\mathcal{O}(N \log N)$ time using $\mathcal{O}(N \log N)$ memory. We perform four matrix-vector multiplications with the four partitions of the matrix and those multiplications are decomposed as

$$\bar{\bar{Z}}_{ab} \cdot x_b = \bar{\bar{Z}}_{ab}^{NF} \cdot x_b + \bar{\bar{Z}}_{ab}^{FF} \cdot x_b \qquad (3)$$

for $a = 1, 2$ and $b = 1, 2$. In (3), near-field interactions denoted by $\bar{\bar{Z}}_{ab}^{NF}$ are calculated directly and stored in memory to perform partial multiplications $\bar{\bar{Z}}_{ab}^{NF} \cdot x_b$, whereas multiplications involving far-field interactions, i.e., $\bar{\bar{Z}}_{ab}^{FF} \cdot x_b$, are performed efficiently using MLFMA. Far-field interactions are further decomposed into two parts as

$$\bar{\bar{Z}}_{ab}^{FF} \cdot x_b = \bar{\bar{Z}}_{ab,o}^{FF} \cdot x_b + \bar{\bar{Z}}_{ab,i}^{FF} \cdot x_b \qquad (4)$$

since MLFMA is applied separately for inner and outer media. In order to calculate far-field interactions, a multilevel tree structure with $\mathcal{O}(\log N)$ levels is constructed by placing the object in a computational cube and recursively dividing the object into subdomains. This way, interactions of the RWG functions that are far from each other can be calculated efficiently in three stages, called aggregation, translation, and disaggregation [11].

For efficient solutions of RBC problems, the number of iterations should be small, in addition to fast matrix-vector mul-
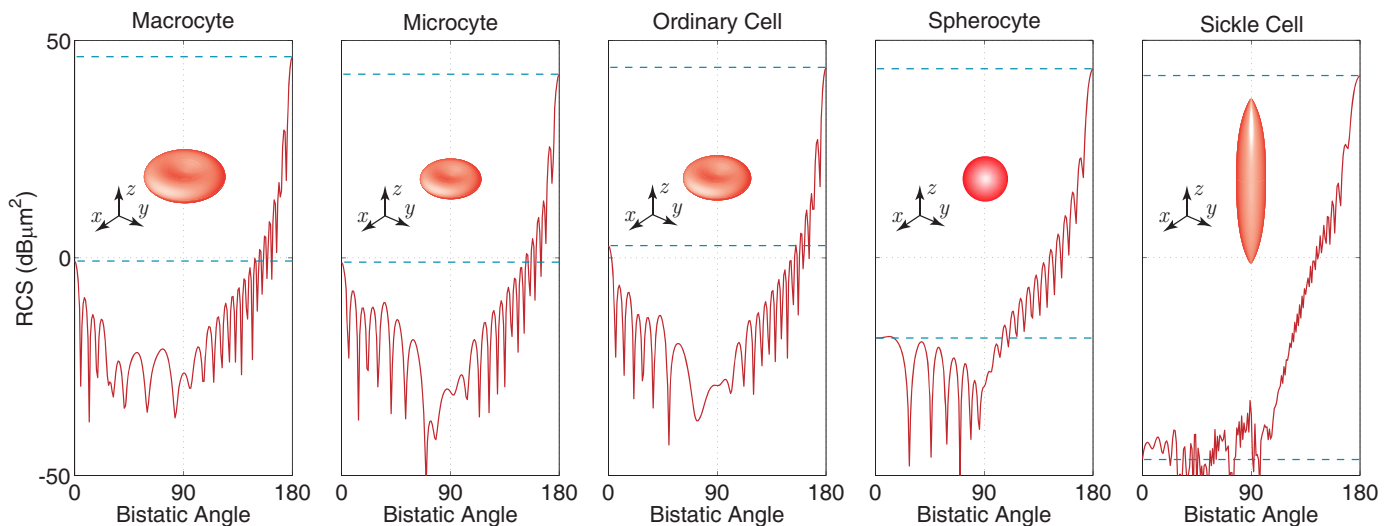
Fig. 1. Bistatic SCS (in dBμm^2) of different RBCs on the z-x plane. RBCs are in default orientation (the axis of the rotational symmetry coincides with the z axis) and they are illuminated by a plane wave propagating in the $-z$ direction with the electric field polarized in the x direction. SCS values in back-scattering ($0°$) and forward-scattering ($180°$) directions are indicated by horizontal dashed lines.

tiplications via MLFMA. Although JMCFIE provides well-conditioned matrix equations that are easy to solve iteratively, we reduce the iteration counts using a four-partition block-diagonal preconditioner (4PBDP) [13], which employs self-interactions of the lowest-level subdomains in MLFMA. The preconditioned matrix equation can be written as

$$\left[\begin{array}{cc} \boldsymbol{B}_{11} & \boldsymbol{B}_{12} \\ \boldsymbol{B}_{21} & \boldsymbol{B}_{22} \end{array}\right]^{-1} \cdot \left[\begin{array}{cc} \bar{\boldsymbol{Z}}_{11} & \bar{\boldsymbol{Z}}_{12} \\ \bar{\boldsymbol{Z}}_{21} & \bar{\boldsymbol{Z}}_{22} \end{array}\right] \cdot \left[\begin{array}{c} \boldsymbol{a}_J \\ \boldsymbol{a}_M \end{array}\right]$$
$$= \left[\begin{array}{cc} \boldsymbol{B}_{11} & \boldsymbol{B}_{12} \\ \boldsymbol{B}_{21} & \boldsymbol{B}_{22} \end{array}\right]^{-1} \cdot \left[\begin{array}{c} \boldsymbol{v}_1 \\ \boldsymbol{v}_2 \end{array}\right], \quad (5)$$

where $\boldsymbol{B}_{ab} \approx \bar{\boldsymbol{Z}}_{ab}$ are block-diagonal matrices.

III. NUMERICAL SOLUTIONS

In this paper, we consider five different RBCs, i.e., an ordinary (healthy) RBC, a macrocyte, a microcyte, a spherocyte, and a sickle cell. The size and the volume of the ordinary RBC, which has a rotationally-symmetric biconcave shape, are 7.70 μm and 80.90 μm^3, respectively. The microcyte and the macrocyte also have biconcave shapes, but their volumes correspond to $5/6$ and $4/3$ of the volume of an ordinary RBC. The spherocyte, which is modelled as a dielectric sphere with 5.36 μm diameter, has exactly the same volume as an ordinary RBC. Finally, the sickle cell also has a rotationally-symmetric shape as the others do, but it is elongated in one dimension. The size of the sickle cell is 20.9 μm, whereas its volume is the same as the volume of an ordinary RBC.

Relative permittivities of RBCs and the host medium are selected as 1.40 and 1.33, respectively. Numerical simulations are performed at 474 THz, corresponding to the output frequency of a typical Helium-Neon laser. RBCs are illuminated by a plane wave propagating in the $-z$ direction with the electric field polarized in the x direction having a unit amplitude. Since the orientation of an RBC can be arbitrary, we investigate various cases for each RBC, except for the spherocyte because it has a fully symmetric geometry. Specifically, in addition to the default orientation, where the axis of the rotational symmetry coincides with the z axis, we perform rotations (typically with $30°$ intervals) around the x axis (θ direction) and around the z axis (ϕ direction), respectively. Hence, multiple values are obtained for each RBC, except for the spherocyte.

Accurate discretizations of RBCs using $\lambda_o/10$ triangles, where λ_o is the wavelength in the host medium, lead to matrix equations involving 180,000–260,000 unknowns. Except for the spherocyte, scattering problems are formulated with JMCFIE and solved iteratively using the biconjugate-gradient-stabilized (BiCGStab) algorithm [14] accelerated via MLFMA. Scattering from the spherocyte is solved exactly by using a Mie-series algorithm. Solutions with MLFMA require 15–20 iterations for 0.001 residual error, and each solution is performed in 3.0–4.5 hours on a 3.6 GHz Intel Xeon processor using 1.5 GB of memory.

IV. RESULTS

Fig. 1 presents the solution of scattering problems involving five different RBCs. The bistatic SCS (in dBμm^2) is plotted on the z-x plane as a function of the observation angle θ from $0°$ (back-scattering direction) to $180°$ (forward-scattering direction). SCS values in back-scattering and forward-scattering directions are indicated by horizontal dashed lines. In this example, RBCs are in default orientation, i.e., the axis of the rotational symmetry coincides with the z axis for each RBC. We note that SCS values obtained for the macrocyte, the microcyte, and the ordinary RBC are very similar to each other.

Fig. 2 presents the bistatic SCS values on the z-x plane when RBCs are rotated by $30°$ angles around the x axis and
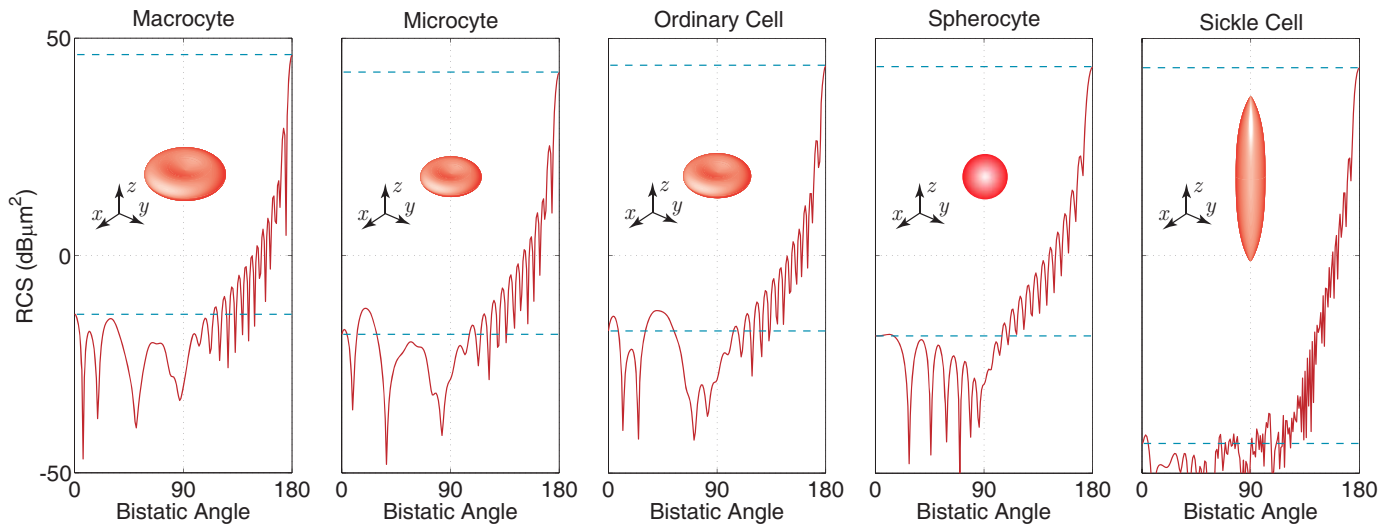
Fig. 2. Bistatic SCS (in $dB\mu m^2$) of different RBCs on the z-x plane. RBCs are rotated by $30°$ angles around the x axis and the z axis, respectively, and they are illuminated by a plane wave propagating in the $-z$ direction with the electric field polarized in the x direction. SCS values in back-scattering ($0°$) and forward-scattering ($180°$) directions are indicated by horizontal dashed lines. Default orientations of the RBCs without rotation are also depicted.
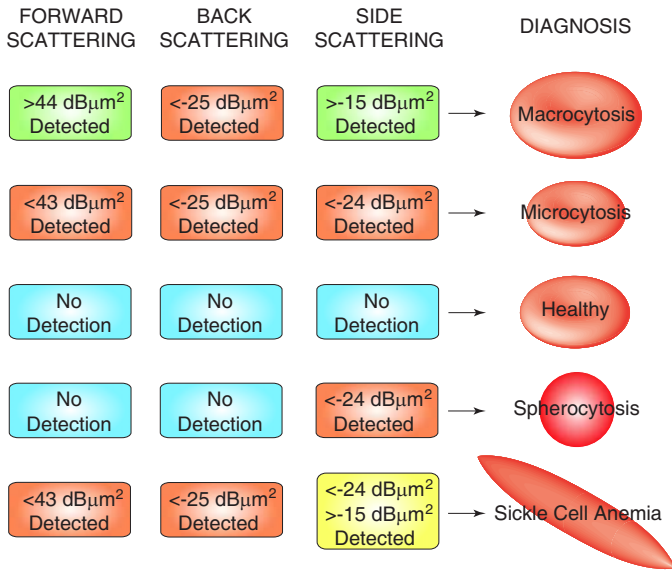

Fig. 3. Diagnosis of various diseases using SCS data.

For a systematic comparison of scattering from different RBC shapes with different orientations, we sample the bistatic SCS on the x-y plane as a function of ϕ. Then, the average SCS value over all the side-scattering directions is computed. This data is combined with SCS values in back-scattering and forward-scattering directions to determine strict guidelines to distinguish diseased RBCs from ordinary ones.

Fig. 3 presents a diagnosis chart based on SCS values obtained in back-scattering, forward-scattering, and side-scattering directions. We summarize the diagnosis of each disease as follows:

- Macrocytosis: Detection of SCS values higher than 44 $dB\mu m^2$ in the forward-scattering direction is a major indicator for macrocytosis.
- Microcytosis: Detection of low SCS values in all directions (back scattering, forward scattering, and side scattering) indicates microcytosis.
- Spherocytosis: Spherocytosis can be diagnosed by the detection of average SCS values lower than -24 $dB\mu m^2$ in the side-scattering direction. As opposed to the microcytosis, SCS values in back-scattering and forward-scattering directions should be in the normal range.
- Sickle-Cell Anemia: Similar to microcytosis, sickle-cell anemia can be diagnosed by the detection of low SCS values in all directions. It can be distinguished from the microcytosis by the detection of average SCS values higher than -15 $dB\mu m^2$ in the side-scattering direction, in addition to low values.

The diagnosis chart in Fig. 3 can be used as a reference for measurements via a diagnosis setup, i.e., a flow cytometer, where SCS values of RBCs are measured via an optical detection system. For a reliable diagnosis, a sufficient number of RBCs should be passed through the setup and the effect of the orientation should be eliminated.

the z axis, respectively. Except for the spherocyte, whose SCS does not change, SCS values are quite different from those obtained for the default orientations. For example, the backscattered SCS decreases significantly for the macrocyte, the microcyte, and the ordinary RBC. In addition, the bistatic SCS from $0°$ to $90°$ becomes less oscillatory when these RBCs are oriented, whereas their SCS values from $90°$ to $180°$ seem slightly affected. Nevertheless, it is difficult to determine a set of rules to distinguish the bistatic SCS values for different RBCs, and comparisons become more complicated when different orientations are considered and included in the analysis.

V. Concluding Remarks

In this paper, we present a comparative study of scattering from healthy and diseased RBCs with deformed shapes. By using a sophisticated simulation environment based on JMC-FIE and MLFMA, scattering problems involving healthy and deformed RBCs are solved both accurately and efficiently. By comparing SCS values in back-scattering, forward-scattering, and side-scattering directions for different RBC shapes and orientations, we are able to determine well-defined guidelines to distinguish deformed RBCs from healthy ones, and hence, to diagnose related diseases.

References

[1] M. Hammer, D. Schweitzer, B. Michel, E. Thamm, and A. Kolb, "Single scattering by red blood cells," *Appl. Opt.*, vol. 37, no. 31, pp. 7410–7418, Nov. 1998.

[2] A. M. K. Nilsson, P. Alsholm, A. Karlsson, and S. Andersson-Engels, "T-matrix computations of light scattering by red blood cells," *Appl. Opt.*, vol. 37, no. 13, pp. 2735–2748, May 1998.

[3] S. V. Tsinopoulos and D. Polyzos, "Scattering of HeNe laser light by an average-sized red blood cell," *Appl. Opt.*, vol. 38, no. 25, pp. 5499–5510, Sep. 1999.

[4] S. V. Tsinopoulos, E. J. Sellountos, and D. Polyzos, "Light scattering by aggregated red blood cells," *Appl. Opt.*, vol. 41, no. 7, pp. 1408–1417, Mar. 2002.

[5] J. He, A. Karlsson, J. Swartling, and S. Andersson-Engels, "Light scattering by multiple red blood cells," *J. Opt. Soc. Am. A*, vol. 21, no. 10, 1953–1961, Oct. 2004.

[6] A. Karlsson, J. He, J. Swartling, and S. Andersson-Engels, "Numerical simulations of light scattering by red blood cells," *IEEE Trans. Biomed. Eng.*, vol. 52, no. 1, 13–18, Jan. 2005.

[7] J. Q. Lu, P. Yang, and X. H. Hu, "Simulations of light scattering from a biconcave red blood cell using the finite-difference time-domain method," *J. Biomed. Opt.*, vol. 10, no. 2, pp. 024022-1–024022-10, Mar./Apr. 2005.

[8] N. K. Uzunoglu, D. Yova, and G. S. Stamatakos, "Light scattering by pathological and deformed erythrocytes: an integral equation model," *J. Biomed. Opt.*, vol. 2, no. 3, 310–318, July 1997.

[9] T. W. Lloyd, J. M. Song, and M. Yang, "Numerical study of surface integral formulations for low-contrast objects," *IEEE Antennas Wireless Propag. Lett.*, vol. 4, 482–485, 2005.

[10] P. Ylä-Oijala and M. Taskinen, "Application of combined field integral equation for electromagnetic scattering by dielectric and composite objects," *IEEE Trans. Antennas Propag.*, vol. 53, no. 3, pp. 1168–1173, Mar. 2005.

[11] J. Song, C.-C. Lu, and W. C. Chew, "Multilevel fast multipole algorithm for electromagnetic scattering by large complex objects," *IEEE Trans. Antennas Propag.*, vol. 45, no. 10, pp. 1488–1493, Oct. 1997.

[12] S. M. Rao, D. R. Wilton, and A. W. Glisson, "Electromagnetic scattering by surfaces of arbitrary shape," *IEEE Trans. Antennas Propag.*, vol. 30, no. 3, pp. 409–418, May 1982.

[13] Ö. Ergül and L. Gürel, "Comparison of integral-equation formulations for the fast and accurate solution of scattering problems involving dielectric objects with the multilevel fast multipole algorithm," *IEEE Trans. Antennas Propag.*, vol. 57, no. 1, pp. 176–187, Jan. 2009.

[14] H. A. van der Vorst, "Bi-CGSTAB: A fast and smoothly converging variant of Bi-CG for the solution of nonsymmetric linear systems," *SIAM J. Sci. Stat. Comput.*, vol. 13, no. 2, pp. 631–644, Mar. 1992.